(Supporting Information)

Advanced Self-powered Visible-light Photodetector Based on Asymmetric $Au/CsPbBr_3/SmB_6$ Junction

Zairan Liu [a], Gang Cao [a], Zhaozhi Guan [a], Yan Tian [a], Jidong Liu [a], Jun Chen [a], Shaozhi Deng [a, *], Fei Liu [a, *]

[a]State Key Laboratory of Optoelectronic Materials and Technologies, Guangdong Province Key Laboratory of Display Material and Technology, School of Electronics and Information Technology, Sun Yat-sen University, Guangzhou, 510275, People's Republic of China

*Corresponding email: liufei@mail.sysu.edu.cn, stsdsz@mail.sysu.edu.cn
Electronic Supplementary Information (ESI) available: [details of any supplementary information available should be included here]. See DOI: 10.1039/x0xx00000x

1. Measurement of the work function of the samples

To conduct the band alignment in the $CsPbBr_3/SmB_6$, KPFM technique was used to measure the surface work function of SmB_6 and $CsPbBr_3$, as presented in Fig. S1(a,b). By calculating the contact potential difference (CPD) between sample and AFM tip, the work function of $CsPbBr_3$ and SmB_6 can be respectively obtained to be 4.3 eV and 4.75 eV based on the equations of $\Phi_{SmB_6} = \Phi_{tip1} + CPD_{SmB_6}$ and $\Phi_{CsPbBr_3} = \Phi_{tip2} + CPD_{CsPbBr_3}$,[1, 2] where Φ_{tip1}=5 eV and Φ_{tip2}=4.3 eV are the work functions of AFM tip 1 and 2, and CPD_{CsPbBr_3}=0.45 eV and CPD_{SmB_6}=-0.7 eV are the contact potential differences between sample and AFM tip. The as-measured work functions of the $CsPbBr_3$ (4.75 eV) and SmB_6 (4.3 eV) are also in good agreement with the reported results in previous works.[3-5]

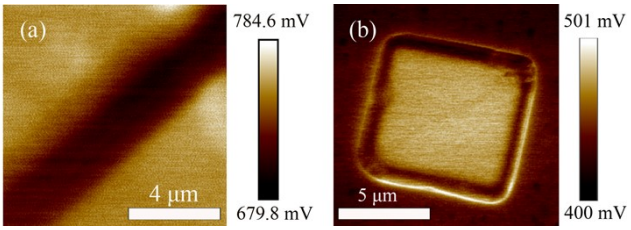

Fig. S1 KPFM characterizations of the as-grown (a) SmB_6 nanobelt and (b) $CsPbBr_3$ microsheet, respectively.

2. Electric transport behaviors of the field effect transistor based on $CsPbBr_3$ or SmB_6

The transfer characteristic curves of the SmB_6 nanobelt at different V_{ds} are shown in Fig. S2(a), where I_{ds} represents the drain-source current, V_g is the gate voltage and V_{ds} stands for the drain-source voltage. It is clearly seen that I_{ds} nearly keeps unvaried with V_g when V_{ds} is 0.2 V, proving that the transport behaviors of SmB_6 is almost independent on the gate voltage and it has metallic behaviors. Subsequently, Figure S2(b) gives the transfer curves of the FET device based on $CsPbBr_3$ microsheet at the drain-source voltage of -2 V. From the transfer curves of the FET, the $CsPbBr_3$ microsheet can be determined to have p-type conductive behaviors and the average hole carrier mobility is about 0.4 $cm^2 V^{-1} s^{-1}$.

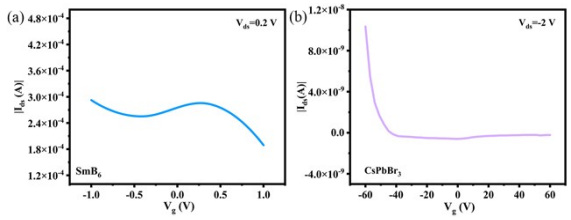

Fig. S2 transfer characteristic curves of the FETs based on (a) SmB_6 nanobelt (b) $CsPbBr_3$ microsheet, respectively.

3. PL decay behaviors of the $CsPbBr_3$ and $CsPbBr_3/SmB_6$ samples

Typical time-resolved PL spectra of a $CsPbBr_3$ microsheet and $CsPbBr_3/SmB_6$ Schottky junction are given in Figure S3 to study the electron-hole population behaviors under 405-nm pulsed irradiation. It is known that the PL decay curve can be regarded as a superposition of fast and slow dynamic components, which should exhibit the time-dependent biexponential behaviors. Accordingly, the PL decay equation can be written as $f(t) = f_1 e^{-t/\tau_1} + f_2 e^{-t/\tau_2}$, [6, 7] where f_1 and f_2 are the constants reflecting the distribution coefficients, t is the diffustion time of the exicton, and τ_1 and τ_2 denote the decay lifetimes of surface exicton and bulk exicton, respectively. Based on Fig. S3, the characteristic fluorescence lifetimes of τ_1 and τ_2 are respectively calculated to be 3.6 ns and 5.7 ns for bare $CsPbBr_3$ microsheet , which are clearly longer than those (1.4 ns and 3.5 ns) for $CsPbBr_3/SmB_6$ Schottky junction. Also, the mean fluorescence lifetime (τ_{ave}) can be worked out by the expression of $\tau_{ave}=\sum f_i\tau_i^2/f_i\tau_i$, [6, 7] where f_i is the distribution coefficient constant and t_i represents the decay time constant. By this way, τ_{ave} is deduced to be respectively 3.6 ns and 2.56 ns for bare $CsPbBr_3$ microsheet and $CsPbBr_3/SmB_6$ junction, suggesting that the recombination efficiency of the electron-hole pairs is greatly reduced while their separation efficiency is remarkably enhanced due to the existence of Schottky junction.

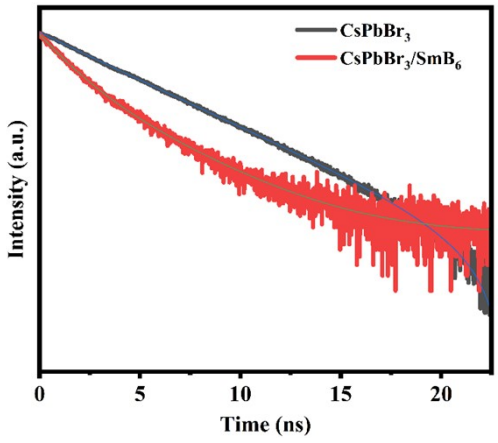

Fig. S3 Typical PL decay curves and biexponential fitting results for the $CsPbBr_3$ microsheet and $CsPbBr_3/SmB_6$ junction under 405-nm pulsed irradiation, respectively.

4. HRTEM characterization of the $CsPbBr_3/SmB_6$ Schottky junction

Low- and high-resolution transmission electron microscope images of the as-grown $CsPbBr_3/SmB_6$ hybrid structure are presented in Fig. S4 (a, b). One can clearly see that the interlayer spacings are respectively 0.42 nm and 0.41 nm for $CsPbBr_3$ microsheet and SmB_6 nanobelt, indexed as the (1 1 0) and (1 0 0) crystal planes according to the Joint Committee on Powder Diffraction Standards (JCPDS) cards of Nos. 18-0364 and 36-1326. The EDX result of the Schottky junction is demonstrated in Fig. S4(c), in which Cs, Pb, Br, Sm, and B elements coexisted in the EDX spectrum, revealing the successful formation of the $CsPbBr_3/SmB_6$ Schottky junction.

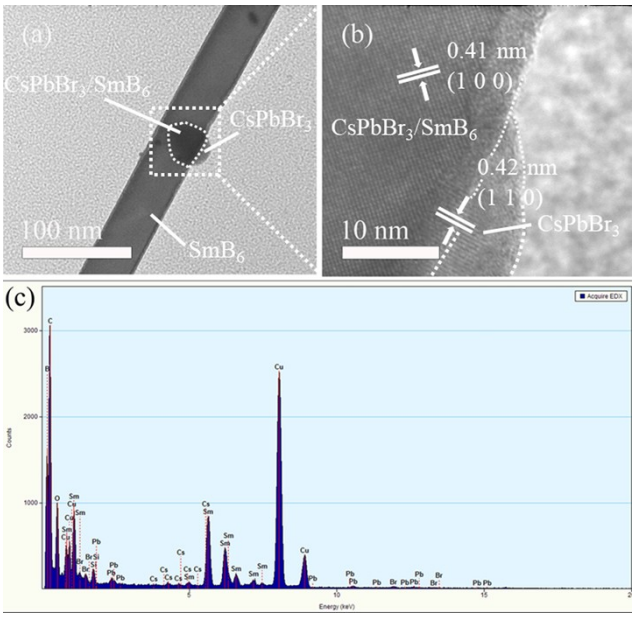

Fig. S4 TEM characterization of the $CsPbBr_3/SmB_6$ Schottky junction. (a, b) Low- and high-magnification TEM images of $CsPbBr_3/SmB_6$. (c) EDX spectrum of the $CsPbBr_3/SmB_6$ junction.

5. Photosensitive behaviors of pristine Au/SmB_6/Au device

Figure S5(a) shows the current-voltage curve of pristine Au/SmB_6/Au nanobelt device under dark and light conditions, and the inset gives the corresponding optical image. By traditional photolithography, pattern Au film with a thickness of 100 nm was deposited on both sides of individual SmB_6 nanobelt as the electrodes, in which their interspacing was about 3 μm. As seen in Fig. S5(a), the I-V curves almost coincide with each other under dark and 514-nm illumination. Also, the time-resolved photoresponse behaviors of the 0.1 V-biased Au/SmB_6/Au under 514-nm irradiation is presented in Fig. S5(b). It is clearly seen that the I-t curve is almost the straight line, unveiling no obvious photoresponse occurs for pristine Au/SmB_6/Au nanobelt and the photosensitive behaviors are absent due to its metal nature.

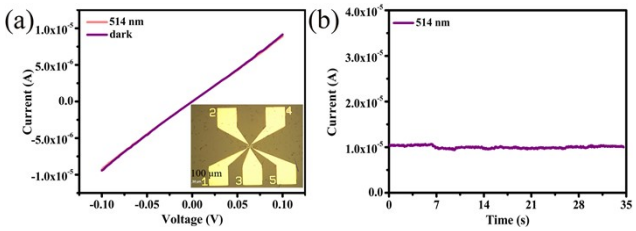

Fig. S5 Photosensitive performances of Au/SmB_6/Au device. (a) The current-voltage curves of Au/SmB_6/Au device under 514-nm light and dark conditions, respectively. The inset gives the optical image of individual Au/SmB_6/Au device. (b) Time-response of the 0.1 V-biased Au/SmB_6/Au device under 514-nm irradiation with a power density of 0.5 mW/cm^2.

Summary table of the photosensitive performances of biased photodetectors based on perovskite

Table SI Summary table of the device performances of perovskite-based photodetectors at biased voltage

Photodetectors	Voltage (V)	Responsivity (A/W)	On/off time (ms)	Specific detectivity (Jones)	*EQE* (%)	Ref.
Au/$CsPbBr_3$/Au	3	0.18	1.0/1.8	6.1×10^{10}	N/A	[8]
Au/$CsPbBr_3$/Au	5	2.776	40/20	N/A	1254	[9]
Au/$CsPbBr_3$/Au	5	0.028	<100	1.8×10^{11}	7	[10]
Au/$CsPbBr_3$@FDTS/Au	5	0.0136	N/A	7.75×10^{10}	N/A	[11]
Au/$CsPbBr_3$(mp-TiO_2)/Au	4	3.5	9000	N/A	N/A	[12]
ITO/$CsPbBr_3$/GaN/Ni/Al	10	1.78	6.6×10^{-5}/0.02	6.5×10^{13}	18.7	[13]
In/$CsPbBr_3$/ZnO/In	-5	0.00063	0.061/1.4	7×10^{9}	N/A	[14]
Au/$CH_3NH_3PbCl_3$/Ag	30	0.24	0.1/2	1.1×10^{11}	73	[15]
Au/$CsPbBr_3$/Au	**4**	**0.029**	**176/80**	$\mathbf{2.6\times10^{10}}$	**7**	**This work**
Au/$CsPbBr_3$/SmB_6	**4**	**4.53**	**42/24**	$\mathbf{3.36\times10^{10}}$	**1095**	**This work**

Supplementary Reference

1. Y. Rosenwaks, R. Shikler, T. Glatzel and S. Sadewasser, *Phys. Rev. B*, 2004, **70**, 085320.
2. X. Wan, E. Chen, J. Yao, M. Gao, X. Miao, S. Wang, Y. Gu, S. Xiao, R. Zhan, K. Chen, Z. Chen, X. Zeng, X. Gu and J. Xu, *Acs Nano*, 2021, **15**, 20319-20331.
3. X. Zeng, S. Li, Z. Liu, Y. Chen, J. Chen, S. Deng, F. Liu and J. She, *Nanomaterials*, 2022, **12**, 4205.
4. F. Zhao, Y. X. Guo, X. Wang, J. H. Tao, J. C. Jiang, Z. G. Hu and J. H. Chu, *Sol. Energy*, 2019, **191**, 263-271.
5. H. Li, Z. P. Li, S. S. Liu, M. Li, X. Y. Wen, J. Lee, S. Lin, M. Y. Li and H. F. Lu, *J. Alloy Compd.*, 2022, **895**, 162570.
6. Z. Shi, S. Li, Y. Li, H. Ji, X. Li, D. Wu, T. Xu, Y. Chen, Y. Tian, Y. Zhang, C. Shan and G. Du, *Acs Nano*, 2018, **12**, 1462-1472.
7. Y. He, L. Matei, H. J. Jung, K. M. McCall, M. Chen, C. C. Stoumpos, Z. Liu, J. A. Peters, D. Y. Chung, B. W. Wessels, M. R. Wasielewski, V. P. Dravid, A. Burger and M. G. Kanatzidis, *Nat. Commun.*, 2018, **9**, 1609.
8. X. Li, D. Yu, F. Cao, Y. Gu, Y. Wei, Y. Wu, J. Song and H. Zeng, *Adv. Funct. Mater.*, 2016, **26**, 5903-5912.
9. W. Zheng, X. Xiong, R. Lin, Z. Zhang, C. Xu and F. Huang, *Acs Appl. Mater. Inter.*, 2018, **10**, 1865-1870.
10. J. Ding, S. Du, Z. Zuo, Y. Zhao, H. Cui and X. Zhan, *J. Phys. Chem. C*, 2017, **121**, 4917-4923.
11. T. Shi, X. Chen, R. He, H. Huang, X. Yuan, Z. Zhang, J. Wang, P. K. Chu and X.-F. Yu, *Adv. Sci.*, 2023, **10**, 2302005.
12. L. Zhou, K. Yu, F. Yang, J. Zheng, Y. Zuo, C. Li, B. Cheng and Q. Wang, *Dalton T.*, 2017, **46**, 1766-1769.
13. L. Su, Y. Zhang and J. Xie, *J. Mater. Chem. C*, 2022, **10**, 1349-1356.
14. L. Su, T. Li and Y. Zhu, *Opt. Express*, 2022, **30**, 23330-23340.
15. J. Yu, J. Zheng, N. Tian, L. Li, Y. Qu, Y. Huang, Y. Luo and W. Tan, *Rsc Adv.*, 2022, **12**, 23578-23583.